Contents lists available at ScienceDirect

Journal of Magnetism and Magnetic Materials

Magnetic induction measurements and identification of the permeability of Magneto-Rheological Elastomers using finite element simulations

Gerlind Schubert, Philip Harrison *

School of Engineering, University of Glasgow, University Avenue, G12 8QQ Glasgow, UK

ARTICLE INFO

ABSTRACT

The isotropic and anisotropic magnetic permeability of Magneto-Rheological Elastomers (MREs) is identified using a simple inverse modelling approach. This involves measuring the magnetic flux density and attractive force occurring between magnets, when MRE specimens are placed in between the magnets. Tests were conducted using isotropic MREs with 10–40% and for anisotropic MREs with 10–30%, particle volume concentration. Magnetic permeabilities were then identified through inverse modelling, by simulating the system using commercially available multi-physics finite element software. As expected, the effective permeability of isotropic MREs was found to be scalar-valued; increasing with increasing particle volume concentration (from about 1.6 at 10% to 3.7 at 30% particle volume concentration). The magnetic permeability of transversely isotropic MRE was itself found to be transversely isotropic, with permeabilities in the direction of particle chain alignment from 1.6 at 10% to 4.45 at 30%, which is up to 1.07–1.25 times higher than in the transverse directions. Results of this investigation are demonstrated to show good agreement with those reported in the literature.

1. Introduction

Magneto-Rheological Elastomers (MREs) belong to a class of smart materials that can change their properties reversibly and almost instantaneously by the application of an external magnetic field. Not only mechanical properties such as stiffness, natural frequency and damping coefficient can be altered, but also the shape and electrical properties of MREs can change. This behaviour is caused by the magnetic interaction of the particles within the matrix material. MREs are promising materials that can potentially be used for a wide range of applications. Experimental analysis and constitutive models are required to predict the complex material behaviour of MREs, and therefore advance the development of applications using MREs. A necessary step in developing accurate constitutive models is a thorough understanding of the magnetic permeability of both isotropic and anisotropic MREs. This requirement provides the motivation behind the current investigation. MREs are particle-reinforced composite materials made of an elastomer as the matrix and usually iron particles as the magnetic component. The magnetisable particles are dispersed in the matrix material, and are locked in position after the

elastomeric material is cured. Both isotropic and anisotropic materials can be prepared. The latter can be manufactured by exposing the uncured composite mixture to a magnetic field during the curing process. This aligns the particles into chains, resulting in both mechanical and magnetic anisotropy. Importantly, the magnetic permeability of anisotropic MREs is no longer a scalar quantity but is more accurately characterised as a tensor property.

So far, MREs have mainly been investigated under small strains; the change of storage modulus and the shift of natural frequency being of particular interest [1–3]. MREs are also known to be magnetostrictive materials [4,5]. From 2009 interest in the magnetic and electrical properties of MREs increased as their potential as sensing materials became recognised [6]. Their electrical resistance was found to increase with increasing magnetic field and increasing compressive force [7–9]. Magnetisation curves of MREs were studied by Boczkowska and Awietjan [10] and the magnetic permeability of anisotropic MREs was investigated by Zeng et al. [11].

In order to develop constitutive models able to predict the behaviour of MREs undergoing large strains, extensive experimental data derived from uniaxial and multi-axial deformation modes are required [12]. Ultimately, the magnetic permeability of MRE materials must also be included in constitutive models if their magnetorheological behaviour is to be fully and accurately predicted. To this end, the focus of the current paper is to

* Corresponding author.
  E-mail address: Philip.Harrison@glasgow.ac.uk (P. Harrison).

characterise the magnetic permeability of MREs. This was done by measuring the magnetic field with a common Gaussmeter and simulating the magnetic field distribution using a finite element simulation.

Various techniques can be used to measure the magnetic permeability of materials, common methods include the *Faraday's* and *Guoy's* scale, which involve measuring force changes due to applied magnetic fields. A modified force balance method was employed by Vicente et al. [13] to measure the magnetic permeability of carbonyl iron powders in suspensions while Nimr et al. [14] measured the mass susceptibility of nanostructured and bulk *LiNiZ*-ferrite samples with a magnetic susceptibility meter and a resonance circuit [15]. *Vibrating sample magnetometry* measures the magnetic induction of an oscillating magnetised sample [16]. The technique was used by Göktürk et al. [17] on a thermoplastic elastomer incorporating ferromagnetic powders and by Bellucci et al. [18] on nickel-zinc ferrites formed by natural rubber. Anisotropic permeability can be measured by extending the method to include torque measurements on the sample; specialised equipment is commercially available to conduct such measurements. However, to the best of the author's knowledge, Zeng et al. [11] presented the first and until now, the only investigation into the magnetic permeability of anisotropic MREs. The magnetic properties of MREs were measured under 1D alternating and 2D rotating magnetic induction excitations, using a single sheet tester. The results of their investigation are included in Fig. 1 and show a large discrepancy with theoretical predictions. Another method is SQUID (Superconducting Quantum Interference Device) magnetometers, they provide a very sensitive way to measure the magnetic properties [19]. Favennec [20] demonstrated the use of inverse modelling using finite element analysis for identification of material properties. Their method required a preliminary sensitivity analysis to determine suitable measurement locations (of temperature in their investigation), before parameter identification via minimisation of an objective function.

The method introduced in this investigation is motivated in part by the constraints imposed by equipment availability but also by the desire to explore novel ideas to measure anisotropic permeability using an inverse finite element modelling strategy. As such, the aims of this investigation are two-fold; the primary objective is to characterise the anisotropic permeability of MREs, while a secondary objective is to examine the viability of using inverse finite element modelling in characterising the anisotropic magnetic permeability of composite materials. Inverse analysis of
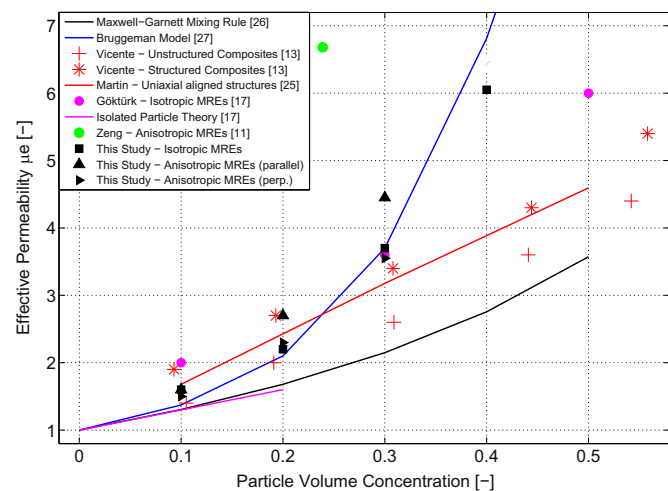

Fig. 1. Effective magnetic permeability, μ_e, versus the volume particle concentration. Theoretical and experimental investigations to determine the magnetic permeability of isotropic and anisotropic composites are compared.

electromagnet fields is already extensively used in imaging subsurface structures in for example, geophysics [21,22], or non-destructive testing [23] and also in identification of material parameters [20]. To the best of the author's knowledge, this is the first time that this technique has been attempted in relation to MREs. A retrospective critical assessment of the advantages and disadvantages of the method is provided in the conclusions section.

The structure of the remainder of the paper is as follows. An overview of theoretical predictions and measurements of the permeability of composites is provided in Section 2. The MRE material and the manufacture process used to prepare this material are described in Section 3. The experimental setup and measurements of both the magnetic field strength and the magnetic attractive force are reported in Section 4. In Section 5, finite element simulations using the commercial multi-physics software, Comsol are reported. The purpose of these simulations was to identify the magnetic permeability of MRE samples. The results are summarised and conclusions are presented in Section 6.

2. Review of the magnetic permeability of composites

To understand the finite element simulation and the identification process carried out (described in Section 5), a brief overview of electromagnetic theory is provided, common methods to measure the magnetic permeability, and prior investigation on the permeability of composites reported in the literature are summarised.

The relation between magnetic induction, **B**, and the magnetic field, **H** in vacuum, in air, or any other non-magnetic environment is constant and defined as

$$\mathbf{B} = \mu_0 \cdot \mathbf{H} \tag{1}$$

where μ_0 is the constant of permeability of a vacuum and has a value of $4\pi \cdot 10^{-7}$ Vs/Am or $1.256 \cdot 10^{-6}$ Vs/Am. The units of **H** are *ampere per meter*, and those of the magnetic induction, **B**, are *Teslas* (*SI* system of units). In a magnetic environment the value of **B** changes and is defined as

$$\mathbf{B} = \mu_0 \boldsymbol{\mu}_r \mathbf{H} \tag{2}$$

where the relative permeability, $\boldsymbol{\mu}_r = \mu/\mu_0$. The permeability $\boldsymbol{\mu}_r$ is unity for a vacuum but can reach values above 1000 for soft magnetic materials such as iron [24]. For magnetically non-linear, ferromagnetic materials such as iron, the permeability, $\boldsymbol{\mu}$, is a function of **H**, and the magnetisation curve, **B**(**H**), is characterised by the initial permeability, $\boldsymbol{\mu}_{in}$, and by the saturation magnetisation, $\mathbf{B}_S$. The permeability of composites (such as MREs) is best described by an effective permeability, $\boldsymbol{\mu}_e$, which is predicted to be far smaller than that of iron [25]. In this work, MREs are assumed to behave magnetically linear with a constant permeability, $\boldsymbol{\mu}_e$, rather than one which is dependant on the magnetic field. As only relatively small magnetic field strengths, **B**, below 0.6 T, were applied in this investigation, this is a reasonable assumption and simplifies all further considerations about the magnetic permeability.

In this investigation both isotropic and anisotropic magnetic permeabilities are considered. For isotropic MREs the permeability is equally defined in all directions with $\mu_{iso} = \mu_X = \mu_Y = \mu_Z$. For anisotropic MREs with the particle alignment in the Z-direction the permeability parallel to the particle alignment is defined with $\mu_{\parallel} = \mu_Z$ and perpendicular to the alignment direction with $\mu_{\perp} = \mu_X = \mu_Y$, analogue for anisotropic MREs with particle alignment in the X-direction $\mu_{\parallel} = \mu_X$ and $\mu_{\perp} = \mu_Y = \mu_Z$, and for the anisotropic MREs with alignment in the Y-direction $\mu_{\parallel} = \mu_Y$ and $\mu_{\perp} = \mu_X = \mu_Z$. Because $\boldsymbol{\mu}$ is anisotropic it can be denoted as

$\boldsymbol{\mu} = \{\mu_X, \mu_Y, \mu_Z\}$ in vector form.

A short review on theoretical and experimental investigations on the permeability of composites is now provided. The well-known three-dimensional *Maxwell–Garnett Mixing Rule* [26] and the *Bruggeman Model* [27] can both be employed to predict the permeability of isotropic composites. Martin et al. proposed a model for the permeability of uniaxially aligned composites [25]. Göktürk et al. [17] presented the *Isolated Particle Theory* for composites with low particle volume fractions. Measurements to obtain the permeability of composites have been reported by Göktürk [17], Vicente [13] and Zeng [11]. A graphical comparison of these prior theoretical and experimental predictions and measurements is presented in Fig. 1. Predictions from all the theoretical models were calculated using an initial permeability for the carbonyl iron particles of $\mu_p = 37$ and for the non-magnetic matrix material of $\mu_m = 1$. For convenience, permeability values measured and identified in the current investigation are also included in the graph (the experimental measurements and the method to identify the permeability are described in Sections 4 and 5).

The measurements performed by Vicente et al. [13] are quite close to the *Maxwell–Garnett Mixing Rule* [26]. However, as stated by Zeng et al. [11], the *Maxwell–Garnett Mixing Rule* does not take the "interaction between the particles into account", which means that permeabilities may well be underestimated. The theoretical approach of Bruggeman [27] considers the interaction of the particles, predicting significantly higher permeabilities especially for larger volume particle concentrations. Measurements on isotropic materials performed by Göktürk et al. [17] show the same tendency as the *Bruggeman* model. Permeabilities determined from the present work also agree very well with the *Bruggeman* model.

3. Material and test specimens

Silicone rubber *MM 240TV* mixed with 30 wt% silicone oil *ACC 34*, both purchased from *ACC Silicones* were used to create the elastomeric matrix material. Carbonyl iron particles (CIP), provided by *BASF*, were used as the magnetisable particles. The particle size ranged from $d_{50} = 3.7$ to 4.7 μm (CIP type SQ). Samples of neat rubber material together with both isotropic and anisotropic MREs, each with volume particle concentrations of 10%, 20%, and 30%, were prepared. Isotropic samples containing 40% particles were also manufactured. All the components were mixed thoroughly for three minutes with a hand mixer before degassing in a vacuum chamber for 10 min. To ensure specimens were free from cavities, the degassing step was conducted twice, once before and once after the mixture was poured into the moulds. The MREs were fast-cured for 1.5 hours at 100 °C. To prepare anisotropic MREs, the mixture inside the moulds was exposed to 400 mT magnetic field strength during the curing process. The direction of the particle alignment was induced in the direction of the applied magnetic field; this was marked on the samples. Optical microscopy revealed uniform particle distribution in isotropic MREs and strong particle alignment in anisotropic MREs [28]. Moulds, made of non-magnetic materials (aluminium and brass), were used to prepare cylindrical samples with a diameter of 29 mm and a height of 13 mm. The final dimensions of the MRE samples were measured three times for each specimen, mean values are given in Table 1.

The samples were found to expand slightly in the direction of their particle alignment, after being removed from the moulds. This meant that for anisotropic samples with horizontal particle alignment, the specimen shape became slightly ellipsoid with their major axis measured along the direction of particle alignment (the major and minor values of the ellipse are provided in Table 1).

Table 1

Averaged dimensions of MRE specimens manufactured. Anisotropic MREs have their particle alignment in the vertical *Z*-direction or the horizontal *X*- or *Y*-direction.

Type of MRE	Diameter (mm)	Height (mm)
Isotropic MREs	28.57	13.35
Anisotropic MREs – *Z*	28.62	13.76
Anisotropic MREs – *X*/*Y*	30.04/27.86	12.98

4. Test setup and experimental measurements

In order to identify the permeability of MRE samples, the magnetic flux density at various positions around the specimen, and the magnetic attractive force between the permanent magnets, was measured. The experimental setup used to measure the magnetic field strength was originally designed to facilitate large-strain uniaxial compression tests [28]. A custom designed test rig manufactured using aluminium and brass was fitted in a universal test machine (*Zwick Z250*). Strong permanent magnets (*Neodymium N52*) were held and taped in position on either side of the MRE sample, with an inter-magnet distance of 33 mm. A view of the rig holding the permanent magnets is shown in Fig. 2a. Test machine, magnets and support rig all remained stationary during the measurements of this investigation. Isotropic and anisotropic samples with differing amounts of iron particles were sequentially placed on the cradle positioned between the magnets (see Fig. 2a). The magnetic flux was measured using a Gaussmeter (*Bell, Type 5180*) at various positions around the specimens. The universal test machine with a 1 kN loadcell measured the attractive force acting between the two permanent magnets. The Gaussmeter setup is shown in Fig. 2a.

To ensure consistent positioning of the Gaussmeter the probe was held by a clamp and the tip of the probe was taped onto the plates of the setup. For the *Top* and *Bottom* positions, the probe was taped on the top and bottom plate of the setup. For *Mid-Height* positions, an aluminium spacer of 6.2 mm height was fixed on the bottom plate and the probe was taped onto this. To illustrate the method, the probe in the *Top01* position is shown in Fig. 2b.

The positions, where the magnetic flux density was measured, are illustrated in the scheme in Fig. 3, and the coordinates of the points are listed in Table 2. The positions of the Gaussmeter probe were measured using a ruler and using photographs.

To ensure repeatable positioning of the different MRE samples, the position was marked on the bottom plate of the setup. Measurements were repeated on three samples of each type of MRE. For anisotropic samples, measurements were taken with particle alignment oriented in the vertical and the two horizontal directions (the samples were rotated by 90°). Measured magnetic field strengths versus iron content for the various MRE samples are plotted in Figs. 4 and 5. Mean values and associated standard deviations are plotted, with each full error bar representing two standard deviations (*i.e.* 1 above and 1 below the mean value). Note that the standard deviations are small and are therefore difficult to see in the figures.

The magnetic flux, B_Z, measured above the MRE samples (*Top* positions) was found to increase with increasing iron content. In contrast the magnetic flux, B_Z, measured at the sides of the MRE samples decreased (*Bottom* and *Mid-Height* positions). As expected, higher iron contents resulted in higher effective permeability (see Fig. 1). This higher magnetic permeability concentrates the magnetic flux lines within the MRE samples, effectively reducing the flux density at the side of the sample. The particle alignment direction in anisotropic MREs plays an important role; as indicated by the experimental results shown in Figs. 4b and 5.
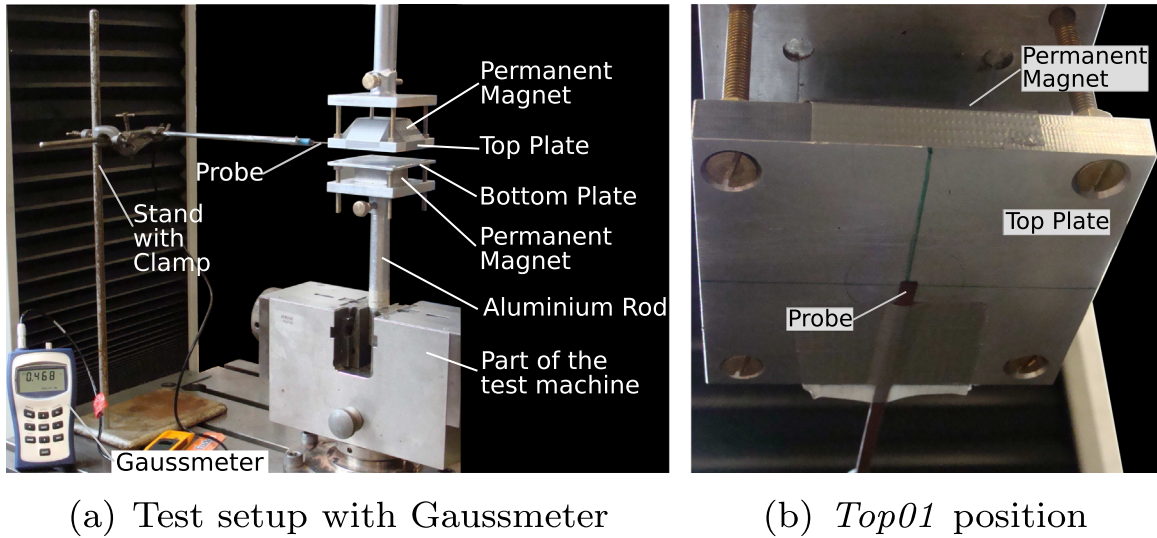
(a) Test setup with Gaussmeter   (b) *Top01* position

Fig. 2. Setup as used for the magnetic field and attractive force measurements. The Gaussmeter probe was hold by a stand and the probe was taped onto position. (a) Test setup with Gaussmeter. (b) *Top01* position.

The increase in magnetic flux density measured above vertically aligned anisotropic MREs, and the decrease in magnetic flux density measured at the side of vertically aligned anisotropic MREs is larger, compared to equivalent measurements on horizontally aligned anisotropic MREs. From this it can be concluded that the magnetic permeability is anisotropic in the anisotropic MREs, with the highest permeability acting in the direction of particle alignment.

The attractive force, *F*, between the permanent magnets, both with and without the specimens placed between the magnets, was measured, and mean values and standard deviations are shown in Fig. 6.

The top magnet was held by the upper rig structure attached to the test machine. To zero the force, the machine cross-head was raised upwards about 50 cm to maximise the distance between the permanent magnets and minimise the influence any magnetic field (measured flux at this upper position was 0 mT). Once the force was zeroed, the test machine cross-head was moved back to the original position, with the permanent magnets positioned 33 mm apart. The force, *F*, measured without an MRE sample between the magnets was 139 N. The same force was measured when a pure rubber sample was placed in the setup. As expected, the attractive force was measured to be higher for specimens with higher iron contents, where anisotropic samples with particle alignment in the vertical direction showed the steepest increase in attractive force.

Table 2
Coordinates of the positions where the magnetic field strength was measured experimentally using a Gaussmeter. The coordinate system is defined in Fig. 3.

Position	x(mm)	y(mm)	z(mm)
Top01	0.5	2.7	17.6
Top02	4.0	4.0	17.6
Botton01	1.2	19.4	0.6
Bottom02	2.4	21.7	0.6
Bottom03	1.1	26.0	0.6
Bottom04	12.6	22.5	0.6
Mid–Height01	0.4	19.0	6.8
Mid–Height02	1.1	21.0	6.8
Mid–Height03	0.8	28.0	6.8
Mid–Height04	9.1	21.0	6.8

5. Prediction of magnetic field using finite element simulations

In order to identify the permeability of the MRE samples, an inverse modelling strategy has been employed. The experimental measurements presented in the previous section have been compared with predictions of magnetic field simulations performed using the multi-physics software, *Comsol* [29]. *Comsol* is a commercially available finite element code, and the *AC/DC* module is specifically designed to simulate magnetic fields. The model geometry defined in the simulations is shown in Fig. 7. The rig itself
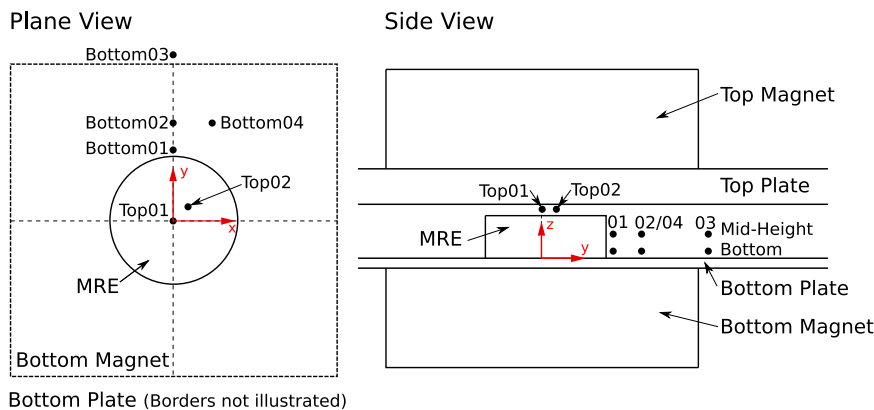

Fig. 3. Scheme showing the positions where the magnetic field strength was measured experimentally using a Gaussmeter.

(a) Isotropic MRE samples

(b) Anisotropic MRE samples with vertical particle alignment (*Z*-direction)
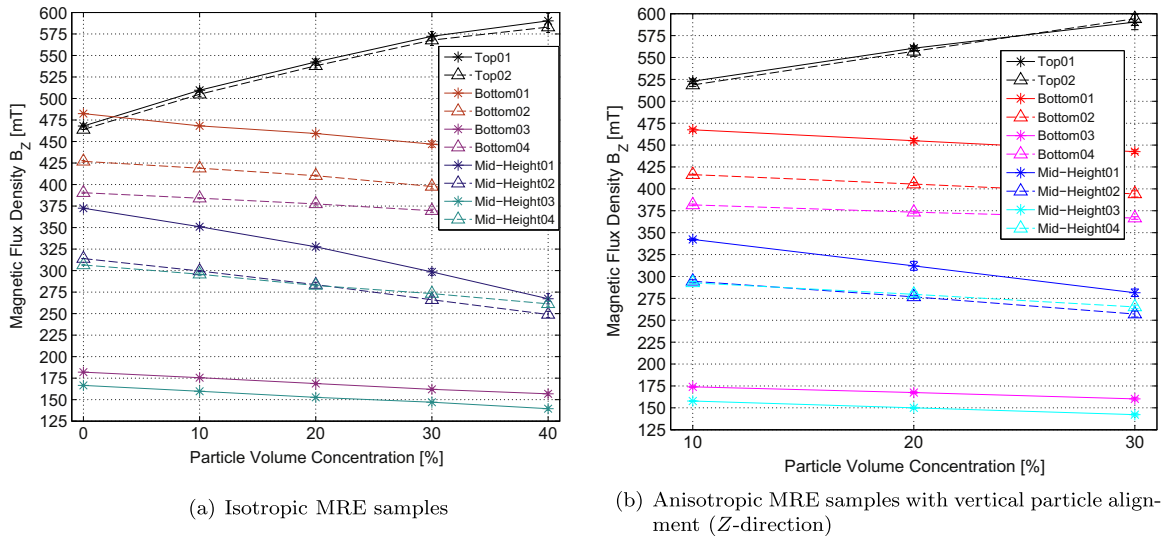
Fig. 4. Results of the magnetic flux measurements with a Gaussmeter at various positions (defined in Fig. 3 and Table 2). Mean values and standard deviations for isotropic MREs and anisotropic MREs with particle alignment in the vertical direction are plotted versus the particle volume concentration. (a) Isotropic MRE samples. (b) Anisotropic MRE samples with vertical particle alignment (*Z*-direction).

was not modelled as this was built of non-magnetic materials and assumed therefore to have no influence on the magnetic field intensity or distribution.

For computational efficiency, a model of just one quarter of the sample and magnets was created using two planes of symmetry. The two magnets were modelled as cubes with rounded corners using a fillet radius of 2 mm to reduce numerical singularities. A magnetisation, *M*, of 1155 kA/m was defined for the magnets [30]. The dimensions of the MRE samples, as listed in Table 1, were used in the numerical *Comsol* model. The volume of air around the magnets and the MRE sample must be defined as a transport medium. As such, a rectangular cuboid was defined with $\mu_r = 1$, as shown in Fig. 7. To ensure the volume was sufficiently large a parametric study was performed, increasing the dimensions of the rectangular cuboid until convergence of the magnetic flux predictions was achieved. A size of $300 \times 300 \times 600$ mm was

determined. The finite element mesh was refined in locations with the highest gradients in field strength. Elements of the mesh in the magnets and the MRE sample measured 3 mm side length, whereas elements at the borders of the rectangular cuboid of air were as large as 60 mm maximum side length, a gradually increasing element size was employed between these two extremes. A mesh convergence study indicated that the mesh provided a good compromise between accuracy and computational efficiency.

To study the magnetic field distribution and to enable comparison with experimental measurements, the magnetic permeability of the MRE sample within the model was adjusted using parametric sweeps. The permeability of the material was defined first as isotropic (with the same value in all directions), and later as anisotropic (with different values in the three orthogonal directions). The experimental measurement locations (defined in Fig. 3 and Table 2) were defined as data collection points in the
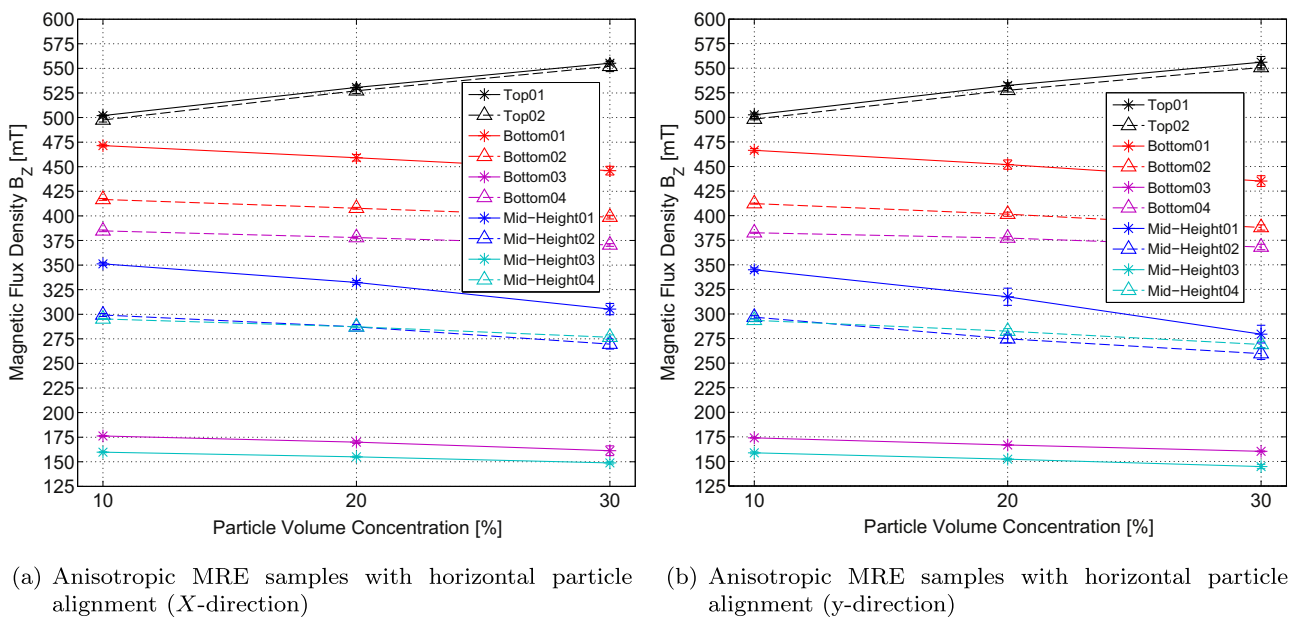

(a) Anisotropic MRE samples with horizontal particle alignment (*X*-direction)

(b) Anisotropic MRE samples with horizontal particle alignment (y-direction)

Fig. 5. Results of the magnetic flux measurements with a Gaussmeter at various positions (defined in Fig. 3 and Table 2). Mean values and standard deviations for anisotropic MREs with particle alignment in the two horizontal directions are plotted versus the particle volume concentration. (a) Anisotropic MRE samples with horizontal particle alignment (*X*-direction). (b) Anisotropic MRE samples with horizontal particle alignment (y-direction).
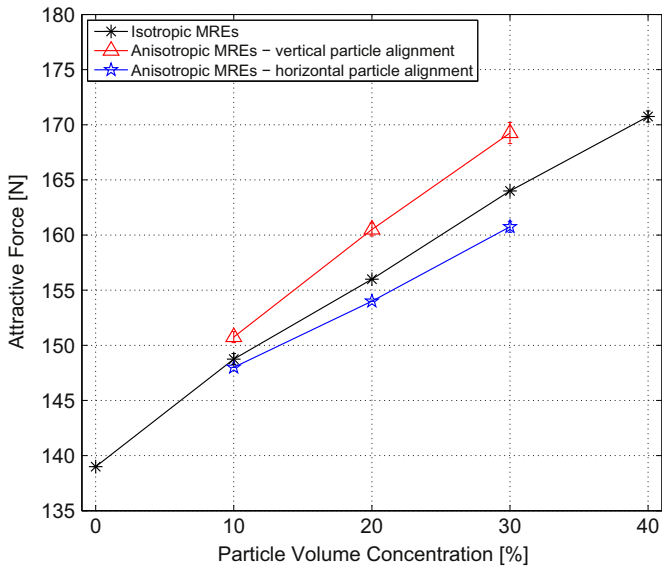
Fig. 6. Results of the attractive force measurements. Mean values and standard deviations for isotropic and anisotropic MREs with particle alignment in vertical and horizontal directions are illustrated versus the particle volume concentration.
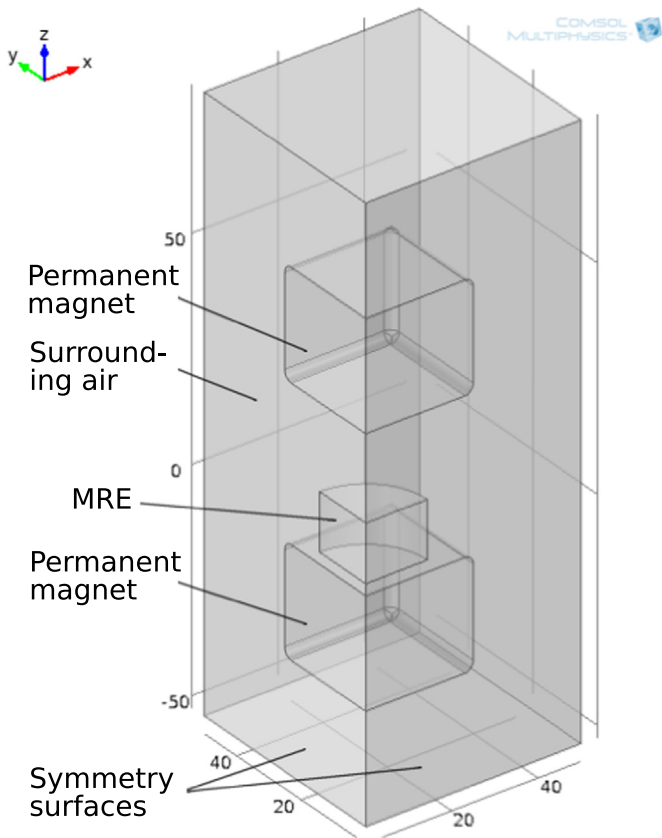

Fig. 7. Geometry with the permanent magnets and the MRE sample defined in the finite element model. Symmetry conditions were applied.

numerical simulations. In this way, the magnetic flux density at the same positions as those used to monitor the flux density in the experiments could be predicted as a function of magnetic permeability. By comparing experimental measurements (B_Z versus particle volume concentration, shown in Figs. 4–6) with the numerical predictions (B_Z versus μ_Z shown in Figs. 8 and 9, and Figs. 11–13), ranges of possible permeabilities μ on each measurement position and for the attractive force results for each type
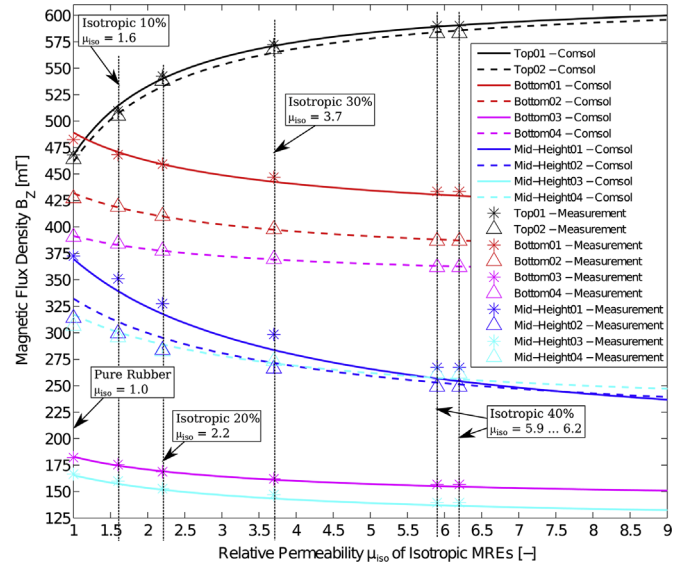

Fig. 8. The magnetic flux density, B_Z, at various positions (Fig. 3 and Table 2) is illustrated versus isotropic permeability μ_{iso}. Average experimentally measured values (Figs. 4a) are plotted using the identified permeabilities μ_{iso} (Table 3). For the case of isotropic MREs with 40 vol% iron volume content a range of magnetic permeabilities was identified: two markers have been used to indicate the lower and upper limit of this range. The text inside the figure lists the results for each isotropic MRE sample.

Fig. 9. The attractive force, F, between the permanent magnets is illustrated versus isotropic permeability μ_{iso}. Average experimentally measured values (Fig. 6) are plotted using the identified permeabilities μ_{iso} (Table 3). For the case of isotropic MREs with 40 vol% iron content a range of magnetic permeabilities was identified: two markers have been used to indicate the lower and upper limit of this range. The text inside the figure lists the results for each isotropic MRE sample.
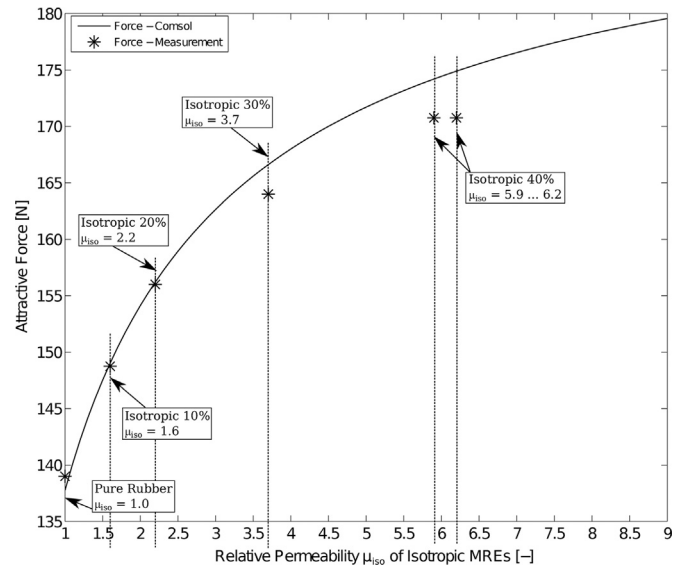
of MRE samples could be identified. Those ranges were narrowed in terms of common intersection ranges to determine isotropic and anisotropic permeabilities for each type of MRE. The identification procedure was performed first for isotropic and later for anisotropic MREs, more details are provided in the following sections.

5.1. Permeability of isotropic MREs

For isotropic MRE samples, only a scalar value of permeability μ_{iso} is required in the numerical simulations. In order to find these
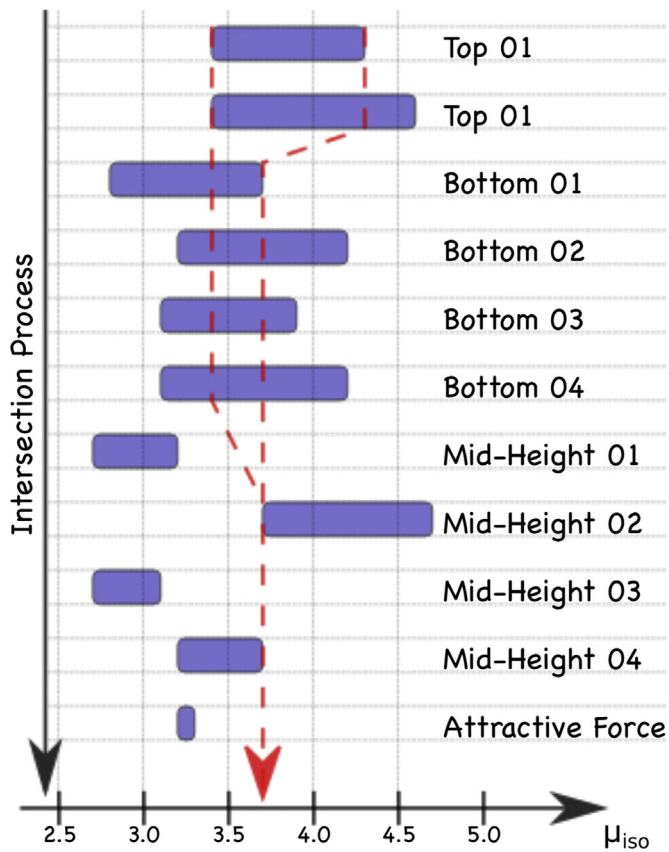
Fig. 10. Intersection process to identify the permeability of an isotropic 30% MRE. The permeability ranges on each position are illustrated as blue boxes, and the intersection process is demonstrated with the red arrow. The identified permeability for the isotropic 30% MREs is $\mu_{iso} = 3.7$. (For interpretation of the references to colour in this figure caption, the reader is referred to the web version of this paper.)

values, a parametric sweep was used to vary the relative permeability, μ_{iso}, from 1 to 10 in increments of 0.1. The magnetic flux density, B_Z, at the various positions and the attractive force, F, between the magnets were then calculated. Numerical predictions of magnetic field, B_Z, versus relative permeability are plotted in Fig. 8 and attractive force, F, versus relative permeability are plotted in Fig. 9. Also included in these figures are measured magnetic field and attraction force values, plotted using the relative permeabilities identified for each sample using the simple fitting process described below.

A range of plausible sample relative permeabilities was identified for each measurement position, by matching numerical predictions of the magnetic field with the experimentally measured range of values (mean values $\pm$ standard deviations). These ranges of permeability are indicated with blue boxes in Fig. 10. Rather than using the typical process of minimising an objective function, an identification process was carried out that involved determining a common intersection range across all fitted permeability ranges found for each measurement position. The intersection process was performed in a specific order, starting from position, Top01, followed by Top02, Bottom01 to Bottom04, and Mid-Height01 to Mid-Height04, and last by the attractive force. The intersection process is indicated with the red dotted arrow in Fig. 10. The permeability ranges found and the intersection process performed on an isotropic 30% MREs are illustrated in Fig. 10 to clarify the identification process.

Note that in some cases, certain experimental data were discarded as they lay outside the intersection range and were judged to be unreliable data points. The Top01 position was chosen as a

starting point for the identification process as the measurements (Fig. 4) and also the simulation results (Fig. 8) showed that the magnetic flux at the Top01 and Top02 positions are close and therefore insensitive to errors in measurement position. The magnetic flux density is uniformly distributed in the centre of the permanent magnets (the location of the two Top positions), whereas the distribution is less uniform close to the edge of the magnets (the location of the Mid-Height and Bottom positions). The experimental measurements of the Top01 and Top02 positions were thus assumed to be the most reliable experimental data points. The values of magnetic flux density at the sides of the sample (Bottom and Mid-Height positions) were found to be much more sensitive to the position and were therefore judged to be of secondary importance during the fitting process. The attractive force, F, between the two permanent magnets is a global value, independent of any measurement position. Only one value was determined for each tested MRE in contrast to the magnetic flux that was measured at 10 different positions. Due to this the attractive force measurements were judged to be the least important values for the intersection process. This specific ordering of data point locations, used in the identification process led to the most inclusive solution, other orderings meant that more data points had to be discarded. The final permeabilities for isotropic MREs are listed in Table 3. In the case of isotropic MREs with 40% iron content a range of permeabilities was identified rather than a unique value.

As mentioned earlier, experimental data measured from isotropic samples with different iron contents are plotted in Figs. 8 and 9 using the identified magnetic permeabilities listed in Table 3. In general, the measurements of magnetic flux density are in very good agreement with predictions from the numerical simulations. Only the measurements at the Mid-Height01 and Mid-Height02 positions disagree, and had to be discarded from the identification process. The attractive force measurements also agree well with numerical predictions for isotropic MREs of 10 and 20% iron content, though the experimental values are slightly lower (by less than 3%) than the force predicted in the numerical simulations for the samples with the higher particle contents, i.e. 30% and 40% iron volume concentration.

5.2. Permeability of anisotropic MREs

In this section, cases of vertical and horizontal particle alignment are each considered in turn. It is shown in this section that both are required to identify final permeabilities, $\mu_{\parallel}$ and $\mu_{\perp}$, of transversely isotropic MREs.

5.2.1. Anisotropic MREs with vertical particle alignment

In order to simulate samples with vertical particle alignment, the magnetic permeability in the numerical model was defined as transversely anisotropic, using values of $\mu_Z = \mu_{\parallel}$ in the vertical direction and $\mu_X = \mu_Y = \mu_{\perp}$ in the two horizontal directions. An inner and outer parametric sweep was performed within the Comsol simulation environment, to calculate the magnetic flux density, B_Z,

Table 3
Identified relative permeabilities, μ_{iso}, for isotropic MRE samples of different particle volume concentrations.

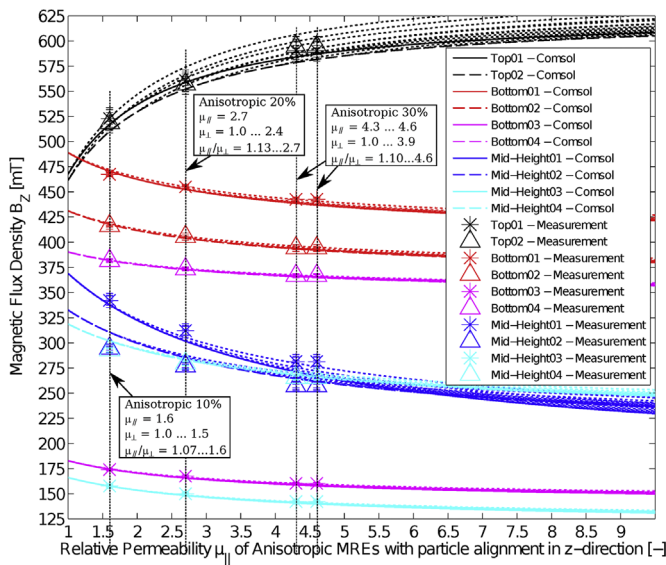| Type of isotropic MRE	μ_{iso} (−)
Isotropic 10% MREs	1.6
Isotropic 20% MREs	2.2
Isotropic 30% MREs	3.7
Isotropic 40% MREs	5.9 to 6.2

Fig. 11. The magnetic flux density, B_Z, at various positions (Fig. 3 and Table 2) is illustrated versus the permeability $\mu_\parallel$ of anisotropic MRE samples with particle alignment in the Z-direction: solid lines represent the isotropic case with $\mu_\parallel = \mu_\perp$ and dotted lines the anisotropic case with $\mu_\parallel > \mu_\perp$. Average experimentally measured values (Figs. 4b) are plotted using the identified permeabilities (Table 4). For the case of anisotropic MREs with 30 vol% iron content a range of magnetic permeabilities was identified: two markers have been used to indicate the lower and upper limit of this range. The text inside the figure lists the results for each anisotropic MRE sample.
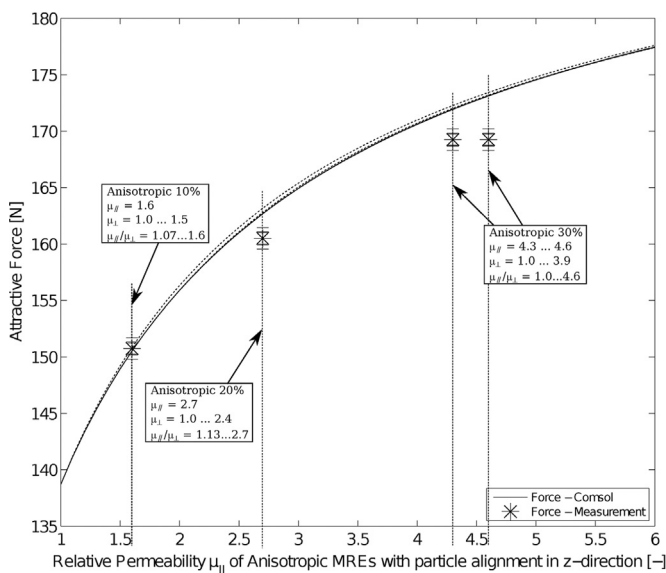
Fig. 12. The attractive force, F, between the permanent magnets is illustrated versus the permeability $\mu_\parallel$ of anisotropic MRE samples with particle alignment in the Z-direction: the solid line represents the isotropic case with $\mu_\parallel = \mu_\perp$ and dotted lines the anisotropic case with $\mu_\parallel > \mu_\perp$. Average experimentally measured values (Fig. 6) are plotted using the identified permeabilities (Table 4). For the case of anisotropic MREs with 30 vol% iron content a range of magnetic permeabilities was identified: two markers have been used to indicate the lower and upper limit of this range. The text inside the figure lists the results for each anisotropic MRE sample.

and the attractive force, F, for all possible combinations of $\mu_\parallel$ and $\mu_\perp$. The sweep was performed using $\mu = 1 - 10$ in increments of 0.1 for both permeabilities. In Fig. 11 predictions of the magnetic flux density, B_Z, and in Fig. 12 predictions of the attractive force are plotted versus the relative permeability, $\mu_\parallel$. Continuous solid lines represent the isotropic case where $\mu_\parallel = \mu_\perp$. The dotted lines represent the anisotropic case with $\mu_\parallel > \mu_\perp$, with $\mu_\parallel$ being the largest

Table 4
Permeabilities, $\mu_\parallel$ and $\mu_\perp$, of anisotropic MRE samples with particle alignment in the Z-direction.

Type of anisotropic MRE	$\mu_\parallel$	$\mu_\perp$
Anisotropic 10% MREs	1.6	1.0…1.5
Anisotropic 20% MREs	2.7	1.0…2.4
Anisotropic 30% MREs	4.3…4.6	1.0…3.9

permeability (note that $\mu_\parallel$ must always be greater than $\mu_\perp$ otherwise the particle alignment direction would change). The dotted lines represent different values of $\mu_\perp$, plotted in increments of 1.

Note that changes in $\mu_\perp$ do not significantly change B_Z, when calculated at the side of the specimen (the dotted lines for the *Bottom* and *Mid-Height* positions are always close to the isotropic case). Relatively large changes in B_Z for different values of $\mu_\perp$ become noticeable only for the positions *Top01* and *Top02*.

Note also, that changes in $\mu_\perp$ do not change the attractive force predictions very much, so the dotted lines in Fig. 12 are hardly visible as all predictions are very close to those of the isotropic case. The permeabilities of anisotropic MREs with vertical particle alignment were identified using a fitting procedure analogous to the identification process described in Section 5.1 and illustrated in Fig. 10. However, in contrast to the process used for the isotropic MREs, here the intersection process was repeated for both $\mu_\parallel$ and $\mu_\perp$. The results are summarised in Table 4.

The possible range of permeabilities determined for $\mu_\perp$ is very large, as changes in predictions of the magnetic flux, B_Z, and the attractive force, F, are both insensitive to changes in $\mu_\perp$ resulting in a large intersection range in the results (see Table 4). Further experiments are therefore required to more accurately determine this range (see Section 5.2.2). In order to compare the numerically determined values of $\mu_\parallel$ with the predictions of the numerical simulations, the average experimental values of B_Z are plotted in Figs. 11 and 12. In the case where a range of permeabilities was determined (*i.e.* MREs with 30% iron content) two markers are used, indicating the upper and lower limits of the possible range. The experimental measurements agree very well with predictions of the numerical simulations. As anticipated, measured values and numerical predictions do not match exactly at the *Mid-Height01* and *Mid-Height02* positions for the same reasons as discussed in Section 5.1 in relation to isotropic MREs.

5.2.2. Anisotropic MREs with horizontal particle alignment

In order to further narrow the range of permeabilities identified in the fitting process reported in Section 5.2.1, the process is repeated with anisotropic MREs having the particle alignment oriented horizontally. In order to calculate the magnetic flux, B_Z, and attractive force, F, two cases were considered: MRE samples with particle alignment in the X-direction and MRE samples with particle alignment in the Y-direction. In the numerical simulations, the permeability was once again defined as being transversely anisotropic, with the largest permeability $\mu_X = \mu_\parallel$ when particle alignment was in the X-direction, and $\mu_Y = \mu_\parallel$ when particle alignment was in the Y-direction. In both cases the two other mutually orthogonal directions were assigned equal permeabilities, $\mu_\perp$. As discussed in Section 3, the shape of the MREs with horizontal particle alignment was slightly ellipsoid: dimensions used in the numerical simulations were adjusted accordingly, and are listed in Table 1. In Fig. 13 predictions of the magnetic flux density, B_Z are plotted versus the relative permeability, $\mu_\perp$, for the anisotropic samples with particle alignment in the X-direction. Continuous solid lines represent the isotropic case where $\mu_\perp = \mu_\parallel$. The dotted lines represent the anisotropic case with $\mu_\perp < \mu_\parallel$. The dotted lines represent different values of $\mu_\parallel$, plotted in increments of 1.
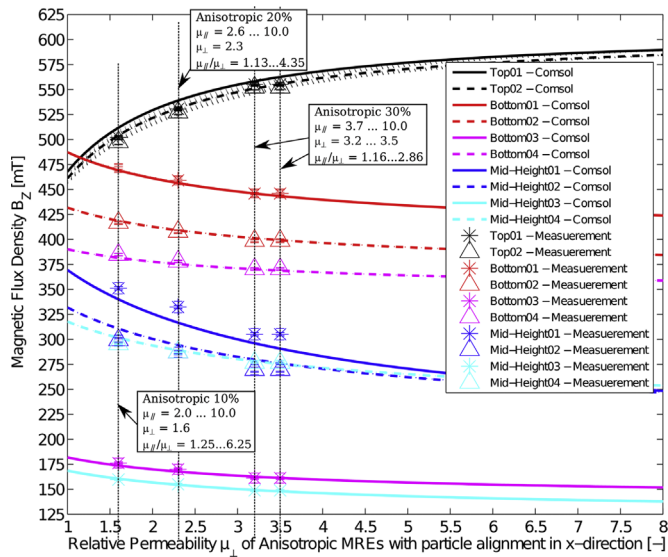
Fig. 13. The magnetic flux density, B_Z, at various positions (Fig. 3 and Table 2) is illustrated versus the permeability $\mu_\perp$ of anisotropic MRE samples with particle alignment in the X-direction: solid lines represent the isotropic case with $\mu_\perp = \mu_\parallel$ and dotted lines the anisotropic case with $\mu_\perp < \mu_\parallel$. Average experimentally measured values (Figs. 5a) are plotted using the identified permeabilities (Table 5). For the case of anisotropic MREs with 30 vol% iron content a range of magnetic permeabilities was identified: two markers have been used to indicate the lower and upper limit of this range. The text inside the figure lists the results for each anisotropic MRE sample.

The same could be done with the attractive force, F, and for predictions with MRE samples with particle alignment in the Y-direction, though for brevity these graphs are omitted here (see [28] for a complete set of graphs). Most of the change in the magnetic field evident in Fig. 13 can be ascribed to changes in $\mu_\perp$ rather than $\mu_\parallel$. The magnetic flux density, B_Z, changes significantly with increasing permeability, $\mu_\perp$, but changing $\mu_\parallel$ produces nearly no variation in B_Z (dotted lines).

To identify the permeabilities the same procedure as that used for isotropic MREs (see Section 5.1 and Fig. 10) and anisotropic MREs with vertical particle alignment (see Section 5.2.1) was used. The identified permeabilities of MREs with particle alignment in X- and Y-directions are listed in Tables 5 and 6, respectively.

Note the large range of possible permeabilities $\mu_\parallel$ in the particle alignment direction; this is due to the insensitivity of B_Z to changes in $\mu_\parallel$. The upper limit 10 listed in Tables 5 and 6 is the maximum permeability used in the numerical simulations. Considered in isolation, experimental data from the MREs with horizontal particle alignment can only be used to determine unique values for permeabilities perpendicular to the alignment direction, $\mu_\perp$.

5.2.3. Permeability of anisotropic MREs

In this section, the results of anisotropic MREs with vertical particle alignment (Section 5.2.1) and with horizontal particle alignment (Section 5.2.2) are combined to identify the final permeabilities $\mu_\parallel$ and $\mu_\perp$ for the transversely anisotropic MREs. The results listed in Table 4 for anisotropic MREs with vertical particle

Table 5
Permeabilities, $\mu_\parallel$ and $\mu_\perp$, of the anisotropic MRE samples with particle alignment in the X-direction.

Type of anisotropic MRE	$\mu_\parallel$	$\mu_\perp$
Anisotropic 10% MREs	2.0…10.0	1.6
Anisotropic 20% MREs	2.6…10.0	2.3
Anisotropic 30% MREs	3.7…10.0	3.2…3.5

Table 6
Permeabilities, $\mu_\parallel$ and $\mu_\perp$, of the anisotropic MRE samples with particle alignment in the Y-direction.

Type of anisotropic MRE	$\mu_\parallel$	$\mu_\perp$
Anisotropic 10% MREs	2.0…10.0	1.7
Anisotropic 20% MREs	2.8…10.0	2.2
Anisotropic 30% MREs	4.3…10.0	3.8

alignment, and listed in Tables 5 and 6 for anisotropic MREs with horizontal particle alignment are combined, and the intersecting permeabilities are taken to be the final values for $\mu_\parallel$ and $\mu_\parallel$. As discussed in Section 5.2.1, permeabilities parallel to the particle alignment are best determined with vertically aligned MRE samples. The lower limits of $\mu_\parallel$ (Tables 5 and 6) agree with the identified $\mu_\parallel$ of vertical aligned samples (Table 4). Only the results of anisotropic samples with 10% iron content are too high. As discussed in Section 5.2.2, permeabilities perpendicular to the particle alignment are best determined with horizontally aligned MRE samples. The upper limits of $\mu_\perp$ (Table 4) agree with the identified $\mu_\perp$ of horizontally aligned MREs (Tables 5 and 6). Only the samples with 10% iron are overestimated in the case of horizontally aligned MRE samples, and as $\mu_\perp$ must be smaller than $\mu_\parallel$ the upper limit from Table 4 has been chosen for the anisotropic 10% MREs. The final permeabilities parallel and perpendicular to the particle alignment are summarised in Table 7. The ratio $\mu_\parallel/\mu_\perp$ is also provided to show the strength of the particle alignment and the resulting magnetic anisotropy.

6. Conclusions

The permeabilities of isotropic and anisotropic MREs were successfully identified by comparing experimental magnetic flux measurements at various positions around the MRE specimen, with calculations of the magnetic flux densities at the same positions predicted by finite element simulations. Ranges of possible permeabilities were determined for each isotropic MRE with 10–40% iron content and for each anisotropic MRE with 10–30% iron content. Mean values of the determined ranges for all types of MREs are summarised in Table 8.

A comparison of the permeabilities determined in this study with results from both theoretical and experimental investigations found in the literature is illustrated in Fig. 1. The identified isotropic permeabilities agree very well with the *Bruggeman* model, and also with measurements performed by Göktürk et al. [17]. The permeabilities of anisotropic MREs with up to 20% iron content are within ranges of those calculated by Martin et al. [25] and are also in agreement with measurements performed by Vicente et al. [13]. The permeabilities of samples with higher iron contents are larger than those found in almost all previous investigations (theoretical and experimentally). Zeng et al. [11] measured even higher permeabilities for anisotropic MREs, though these were higher significantly than all theoretical predictions. The permeability of

Table 7
Final permeabilities $\mu_\parallel$ and $\mu_\perp$ of anisotropic MRE samples. The minimum and maximum ratio $\mu_\parallel/\mu_\perp$ is provided to show the strength of particle alignment and resulting anisotropy.

Type of anisotropic MRE	$\mu_\parallel$	$\mu_\perp$	Ratio $\mu_\parallel/\mu_\perp$
Anisotropic 10% MREs	1.6	1.5	1.07
Anisotropic 20% MREs	2.7	2.2…2.4	1.13…1.23
Anisotropic 30% MREs	4.3…4.6	3.2…3.9	1.10…1.44

Table 8
Mean values of the identified permeabilities for isotropic MREs, μ_{iso}, and for anisotropic MREs in particle alignment direction, $\mu_\parallel$, and perpendicular to the alignment direction, $\mu_\perp$.

Type of MRE	$\mu_{iso}/\mu_\parallel$	$\mu_\perp$
Isotropic 10% MREs	1.60	
Isotropic 20% MREs	2.20	
Isotropic 30% MREs	3.70	
Isotropic 40% MREs	6.05	
Anisotropic 10% MREs	1.60	1.50
Anisotropic 20% MREs	2.70	2.30
Anisotropic 30% MREs	4.45	3.55

anisotropic MREs perpendicular to the particle alignment are below those in the alignment direction, and are very close to the permeabilities of isotropic MREs. This is a reasonable result.

To the best of the author's knowledge, this is the first time this inverse modelling approach has been used to measure the anisotropic permeability of anisotropic MREs and so some consideration of the relative strengths and weaknesses of the method are in order. Disadvantages might include the time involved in collecting data from numerous locations around the samples and the inevitable positioning errors involved in placing the Gaussmeter probe. Postprocessing the final data was a time consuming process and is another drawback of the method. Perhaps also, the time and effort required to develop sufficient expertise to conduct the necessary finite element simulations could be viewed as a disadvantage of the approach, though conversely, the depth of understanding conferred in performing such simulations could arguably be considered one of the technique's main strengths. Continuing with other advantages of the method; the experimental setup is very simple involving just two permanent magnets, a Gaussmeter and a universal test machine. This makes it a relatively inexpensive technique that can be conducted in most mechanical test labs.

Assessing the accuracy of the approach is difficult as only one other investigation [11] has attempted to measure the anisotropic permeability of MREs and those results appear to be significantly different to data gathered in this investigation. However, the compatibility of the data measured in this investigation with the global magnetic fields predicted in the numerical simulations provides strong confidence in the reliability of the results. Good agreement with theoretical predictions, as shown in Fig. 1, reinforces this confidence and effectively provides the first experimental validation of analytical theories describing the magnetic properties of MREs. In future, such experimental data and validated theoretical predictions will be valuable in developing accurate constitutive models capable of describing the behaviour of MRE-based products and applications in response to applied magnetic fields.

Acknowledgments

References

[1] M. Jolly, J. Carlson, B. Munoz, T. Bullions, The magnetoviscoelastic response of elastomer composites consisting of ferrous particles embedded in a polymer matrix, 7 (1996) 613–622, Journal of Intelligent Material Systems and Structures. http://dx.doi.org/10.1177/1045389X9600700601.
[2] J. Ginder, M. Nichols, L. Elie, J. Tardiff, Magnetorheological elastomers: properties and applications, in: Smart Structures and Materials, 1999. http://dx.doi. org/10.1117/12.352787.
[3] M. Lokander, Performance of magnetorheological rubber materials (Doctoral thesis), Department of Fibre and Polymer Technology Royal Institute of Technology Stockholm, 2004. URL ⟨www.diva-portal.org/smash/get/diva2:8859/FULLTEXT01.pdf⟩.
[4] X. Gong, G. Liao, S. Xuan, Full-field deformation of magnetorheological elastomer under uniform magnetic field, 100, 2012, Applied Physics Letters. http://dx.doi.org/10.1063/1.4722789.
[5] G. Diguet, E. Beaugnon, J. Cavaille, Shape effect in the magnetostriction of ferromagnetic composite, 322 (2010) 3337–3341, Journal of Magnetism and Magnetic Materials. http://dx.doi.org/10.1016/j.jmmm.2010.06.020.
[6] W. Li, K. Kostidis, X. Zhang, Y. Zhou, Development of a force sensor working with MR elastomers, in: IEEE/ASME International Conference on Advanced Intelligent Mechatronics, AIM, IEEE, 2009. http://dx.doi.org/10.1109/AIM.2009.5230010.
[7] I. Bica, Compressibility modulus and principal deformations in magnetorheological elastomer: the effect of the magnetic field, 15 (2009) 773–776, Journal of Industrial and Engineering Chemistry. http://dx.doi.org/10.1016/j.jiec.2009.09.028.
[8] I. Bica, Magnetoresistor sensor with magnetorheological elastomers, Journal of Industrial and Engineering Chemistry, 17 (2011) 83–89. http://dx.doi.org/10.1016/j.jiec.2010.12.001.
[9] X. Wang, F. Gordaninejad, M. Calgar, Y. Liu, J. Sutrisno, A. Fuchs, Sensing behavior of magnetorheological elastomers, 131, 2009, Journal of Mechanical Design. http://dx.doi.org/10.1115/1.3160316.
[10] A. Boczkowska, S. Awietjan, Microstructure and properties of magnetorheological elastomers, Advanced Elastomers - Technology, Properties and Applications, D.Sc. Anna Boczkowska (Ed.), ISBN: 978-953-51-0739-2, InTech, 2012. http://dx.doi.org/10.5772/50430.
[11] J. Zeng, Y. Guo, Y. Li, J. Zhu, J. Li, Two-dimensional magnetic property measurement for magneto-rheological elastomer, 113, 2013, Journal of Applied Physics, http://dx.doi.org/10.1063/1.4796046.
[12] R. Ogden, G. Saccomandi, I. Sgura, Fitting hyperelastic models to experimental data, 34 (2004) 484–502, Computational Mechanics. http://dx.doi.org/10.1007/s00466-004-0593-y.
[13] J.d. Vicente, G. Bossis, S. Lacis, M. Guyot, Permeability measurements in cobalt ferrite and carbonyl iron powders and suspensions, 251 (2002) 100–108, Journal of Magnetism and Magnetic Particles. http://dx.doi.org/10.1016/S0304-8853(02)00484-5.
[14] M.E. Nimr, B. Moharram, S. Saafan, S. Assar, Particle size distribution, magnetic permeability and dc conductivity of nano-structured and bulk LiNiZn-ferrite samples, J. Magn. Magn. Mater. 322 (2010) 2108–2112.
[15] D.E. Kony, S. Saafan, Study of the temperature dependence of both permeability and selectivity of Mg Zn hexaferrites, J. Magn. Magn. Mater. 267 (2003) 46–52.
[16] J.J. Morton, Magnetic Properties of Materials—Part 3: Measurements and Applications, University College London, 2012, p. 12.
[17] H. Göktürk, T. Fiske, D. Kalyon, Electric and magnetic properties of a thermoplastic elastomer incorporated with ferromagnetic powders, 29 (1993) 4170–4176, IEEE Transactions on Magnetics. http://dx.doi.org/10.1109/20.280866.
[18] F.S. Bellucci, F.C.L. de Almeida, M.A.L. Nobre, M.A. Rodrguez-Perez, A.T. Paschoalini, A.E. Job, Magnetic properties of vulcanized natural rubber nanocomposites as a function of the concentration, size and shape of the magnetic fillers, Compos. Part B 85 (2016) 196–206.
[19] P. Marcon, K. Ostanina, Overview of methods for magnetic susceptibility measurement, in: PIERS Proceedings, 2012.
[20] Y. Favennec, V. Labb, Y. Tillier, F. Bay, Identification of magnetic parameters by inverse analysis coupled with finite-element modeling, IEEE Trans. Magn. 38 (2002) 3607–3619.
[21] L. Marello, J. Ebbing, L. Gernigon, Magnetic basement study in the barents sea from inversion and forward modelling, Tectonophysics 493 (2010) 153–171.
[22] C. Jiang, M. Mller-Petke, J. Lin, U. Yaramanci, Imaging shallow three dimensional water-bearing structures using magnetic resonance tomography, J. Appl. Geophys. 116 (2015) 17–27.
[23] D. Mukherjee, S. Saha, S. Mukhopadhyay, Inverse mapping of magnetic flux leakage signal for defect characterization, NDT&E Int. 54 (2013) 198–208.
[24] D. Jiles, Introduction to Magnetism and Magnetic Materials, Chapman & Hall, London, 1998.
[25] J. Martin, R. Anderson, D. Read, G. Gulley, Magnetostriction of field-structured magnetoelastomers, vol. 74, Phys. Rev. E, American Physical Society, 2006. http://dx.doi.org/10.1103/PhysRevE.74.051507.
[26] A. Sihvola, I. Lindell, Homogenisation problems of mixtures involving non-isotropic constituent materials, Electromagnetics Laboratory, Helsinki University of Technology, 1997. URL ⟨www.maths.gla.ac.uk/events/tropics/proc/ps/P70_SIH2.PS⟩.
[27] D. Bruggeman, Berechnung verschiedener physikalischer Konstanten von heterogenen Substanzen, vol. 416, Dielektrizitaetskonstanten und Leitfaehigkeiten der Mischkoerper aus isotropen Substanzen: Annalen der Physik, WILEY-VCH Verlag, 1935, pp. 636–664. http://dx.doi.org/10.1002/andp.19354160705.
[28] G. Schubert, Manufacture, Characterisation and modelling of magneto-rheological elastomers (Ph.D. thesis), University of Glasgow School of Engineering, 2014.
[29] Comsol, Comsol Multiphysics 4.2 Documentation, © 1998-2011 COMSOL, 2011. URL ⟨http://www.comsol.com/comsol-multiphysics⟩, retrieved 06/2014.
[30] Supplier: First4Magnets, Technical Data of Neodymium N52 Magnets 50 × 50 × 25 mm, 2011. URL ⟨www.first4magnets.com⟩.